

Composite hindered and restricted model of diffusion (CHARMED) MR imaging of the human brain

Yaniv Assaf^{a,b,*} and Peter J. Basser^c

^aFunctional Brain Imaging Unit, The Wohl Institute for Advanced Imaging, Tel Aviv Sourasky Medical Center, Tel Aviv, Israel

^bDepartment of Neurobiochemistry, Faculty of Life Sciences, Tel Aviv University, Ramat Aviv, Tel Aviv, Israel

^cSection on Tissue Biophysics and Biomimetics, Laboratory of Integrative and Medical Biophysics, National Institute of Child Health and Human Development, The National Institutes of Health, Bethesda, MD 20892-5722, USA

Received 15 August 2004; revised 11 January 2005; accepted 29 March 2005
Available online 24 June 2005

High b value diffusion-weighted images sampled at high angular resolution were analyzed using a composite hindered and restricted model of diffusion (CHARMED). Measurements and simulations of diffusion in white matter using CHARMED provide an unbiased estimate of fiber orientation with consistently smaller angular uncertainty than when calculated using a DTI model or with a dual tensor model for any given signal-to-noise level. Images based on the population fraction of the restricted compartment provide a new contrast mechanism that enhances white matter like DTI. Nevertheless, it is assumed that these images might be more sensitive than DTI to white matter disorders. We also provide here an experimental design and analysis framework to implement CHARMED MRI that is feasible on human clinical scanners.

© 2005 Elsevier Inc. All rights reserved.

Keywords: Diffusion; Restricted; Hindered; DTI; q space; White matter; MRI

Introduction

Magnetic Resonance Imaging (MRI) has significantly improved the radiological assessment of white matter (Filley, 2001). T_1 - and T_2 -weighted and magnetization transfer (MT) MRI have been used to increase image sensitivity to lipids or macromolecules in white matter, which has been attributed to the myelin sheath surrounding axons (Tofts, 2003). Another MR method, diffusion tensor imaging (DTI), increases white matter conspicuity primarily through its sensitivity to the geometrical packing and architectural organiza-

tion of white matter fibers (Basser, 2002; Basser and Pierpaoli, 1996; Basser et al., 1994; Pierpaoli et al., 1996).

DTI yields a diffusion tensor from measurements of the apparent diffusion coefficient (ADC) of water molecules obtained along multiple directions. This measurement can be used to estimate the principal diffusivities parallel and perpendicular to coherent fiber bundles (Basser and Jones, 2002; Basser and Pierpaoli, 1996; Basser et al., 1994; Pierpaoli et al., 1996). Due to the high packing density of axons in fasciculi, the motion perpendicular to axons is more tortuous than that parallel to them. Using the principal diffusivities, it is also possible to calculate the orientationally averaged (or mean) ADC and the degree of diffusion anisotropy (Basser et al., 1994), for which the most popular parameter used presently is the fractional anisotropy (FA) (Basser, 1995).

A typical voxel in a diffusion MRI experiment is of the order of 10 mm^3 , and thus contains thousands of cells and tissue components. The diffusion of water molecules in each compartment (e.g., extracellular space, cell soma, axons, dendrites) is affected by the local viscosity, composition, geometry, and membrane permeability. Of these factors, geometry and permeability appear to have the most pronounced effect on the measured signal because the path that molecules traverse within typical diffusion times in a DTI experiment is larger than these compartment sizes, so that the long-time (tortuosity) limit is achieved. Indeed, since the first applications of diffusion imaging to neuronal tissue in the mid-80s, a significant amount of data has led to the observation that besides the cellular viscosity, permeability and tissue geometry significantly affect water diffusion. It is well known that the diffusivity across red blood cells that are very permeable to water molecules is much higher than other tissue cells (e.g., neurons). Furthermore, the fact that fiber directionality can be measured in white matter implies that the geometrical arrangement of the tissue also contributes significantly to the observed diffusivity.

Diffusion experiments are usually performed by spatially labeling spins at two different times during an MR experiment. These labeling periods are separated by a time interval (known also

* Corresponding author. Department of Neurobiochemistry, Faculty of Life Sciences, Tel Aviv University, Ramat Aviv, Tel Aviv 69978, Israel. Fax: +972 3 6973080.

E-mail address: asafyan@zahav.net.il (Y. Assaf).

Available online on ScienceDirect (www.sciencedirect.com).

as the diffusion time, Δ) during which we measure the spin's displacement. The measured signal decay will depend on the strength of the labeling (referred to as the q value) and the diffusion time. Sometimes, the signal decay is characterized by a b value ($b = q^2\Delta$). An analytic relation between the signal decay and the diffusivity can be found for cases of free, Gaussian diffusion where we use the b factor to calculate the diffusivity ($E = e^{-bD}$, also known as the Stejskal–Tanner equation). In cases of non-Gaussian diffusion, however, it is preferable to describe the signal decay as a function of the q value. Conventional diffusion MRI (including DTI) averages random motions of water molecules in all tissue compartments and is insensitive to exchange (Basser and Jones, 2002). Yet, a Gaussian displacement distribution adequately describes the random motion of water molecules in brain tissue (both gray and white matter) only at low b or q values (Basser, 2002), so that over that range of b (or q) values, the description of the diffusion process using the Stejskal–Tanner equation is meaningful. However, these observations preclude the possibility that DTI alone can tease apart contributions from the intra- and extra-axonal compartments in white matter.

Several years ago, non-Gaussian diffusion was observed in neuronal tissues using strong diffusion weighting (DW) that sensitizes the image to molecular motions on a small length scale ($<2 \mu\text{m}$) (Assaf and Cohen, 1998; Assaf et al., 2002a; Niendorf et al., 1996). This approach revealed a pool of water molecules that is highly anisotropic and restricted, which was attributed mainly to water residing in the intra-axonal space (Assaf and Cohen, 2000). The measurement of water diffusion at high b values was first quantified using q space MR, a model-free analysis of the signal decay, which can provide a displacement probability distribution function in three dimensions (Callaghan, 1991; Cory and Garroway, 1990; King et al., 1997). High b value diffusion imaging complements DTI, in particular, providing information about water mobility in highly restricted compartments (Assaf et al., 2002a). This additional information has been useful in detecting several white matter pathologies (Assaf et al., 2002a,b,c). If a significant portion of the signal observed at high b value originates from restricted motion of intra-axonal water, then it could provide new information about axonal morphology and microstructure not provided by DTI, and could potentially improve the delineation of white matter tracts, as well as white matter assessment in disease and development.

Recently, a composite hindered and restricted model of diffusion (CHARMED) was proposed to provide a more complete physical description of the diffusion process in white matter, expressing the signal decay observed in white matter in terms of Gaussian (hindered) and non-Gaussian (restricted) contributions (Assaf et al., 2004). The model assumes that one contribution to the net signal decay arises from hindered diffusion in the extra-axonal volume (including extra- and intracellular spaces), while another contribution to the net signal decay arises from restricted diffusion in the intra-axonal volume.

In this work, we use CHARMED MRI to characterize 3-D hindered and restricted diffusion in human brain in vivo. Here, we propose an experimental framework for performing CHARMED MRI in vivo within a clinically feasible timeframe, which entails acquiring DW MRIs with multiple b values and multiple gradient directions. We compare the ability of CHARMED MRI and DTI to separate multiple fiber orientations within a single voxel, and describe the biological significance of different microstructural and physical parameters measured (estimated) from CHARMED MRI.

Methods

MRI experiments

MR imaging was performed on a 3-T whole-body Signa Horizon MRI system (GE Medical Systems, Milwaukee) equipped with 40 mT/m gradient coil with a slew rate of $\sim 200 \mu\text{s}$. Five healthy subjects with no history of neuronal disorders were included in this study. The local Institutional Review Board (IRB) approved the experimental protocol; all subjects signed an informed consent form.

The DWI data set consisted of 10 slices of 3 mm thickness with no gap covering 30 mm. Three slices were placed above the top edge of the corpus callosum and the rest below it. The DWIs were acquired with a diffusion-weighted echo-planar imaging sequence (DW-EPI) with the following parameters: TR/TE = 2700/133 ms, $\Delta/\delta = 53/47$ ms, $G_{\text{max}} = 3.4$ Gauss/cm and 2 averages (NEX). The field-of-view (FOV) was 19 cm, matrix size was 64×64 giving a resolution of $3 \times 3 \times 3 \text{ mm}^3$. We acquired one dummy scan prior to each acquisition. The experiment was repeated for 169 diffusion gradient strengths and directions (as specified in Table 1) so that high and low b value images were interleaved. The b value was controlled by changing the gradient amplitude. The number of gradient directions increased at higher b values. For each b value, the diffusion gradient directions were uniformly and symmetrically distributed over a sphere. For each b value shell, as shown in Table 1, a different number of gradient directions was applied, which increased as the b value increased. This was done as we assumed that higher angular resolution is needed at higher b values to detect features of the “intra-axonal” signal. To increase the angular resolution further, we used a different gradient sampling scheme in each b value shell. For instance, the 30 gradient directions at a b value of 8571 s/mm^2 were different from the 30 directions used at a b value of $10,000 \text{ s/mm}^2$. The total acquisition time for the DWI data set was 17 min. Images with $b = 0$ were acquired eight times (every 80 s). These were used for estimating head movement during the scan. Statistical Parametric Mapping (SPM 2) software was used to correct for head movement based on the $b = 0$ images.

Data analysis

Data were analyzed using the CHARMED framework described previously (Assaf et al., 2004), which uses a diffusion tensor to characterize 3-D hindered diffusion in the extra-axonal spaces, and a new 3-D model of restricted diffusion to describe

Table 1
CHARMED gradient direction scheme

b value (s/mm^2)	No. of directions
0	1
714	6
1428	6
2285	12
3214	12
4286	16
5357	16
6429	20
7500	20
8571	30
10,000	30

diffusion in the intra-axonal spaces. The restricted compartment is itself decomposed into a signal arising from motions parallel and perpendicular to impermeable cylindrical axons. Diffusion within the axon parallel to its axis is free and modeled using the 1-D Stejskal–Tanner equation (Stejskal and Tanner, 1965). Diffusion perpendicular to the fibers, however, is restricted and, for a constant gradient experiment, can be modeled using the theory of Neuman et al. (Neuman, 1974) for $\Delta \sim \delta$ (where Δ is the diffusion time and δ is the duration of the diffusion gradient), which is approximately satisfied for many diffusion-weighted MRI sequences used in clinical scanners. The general form of the model is given in Eq. (1) where f_h and f_r are the T_1 - and T_2 (relaxation)-weighted population fractions of the hindered and restricted terms, respectively; $q_{||}$ and q_{\perp} are the components of the \mathbf{q} vector parallel and perpendicular to the fibers, respectively; $\lambda_{||}$ and λ_{\perp} are the eigenvalues of the diffusion tensor parallel and perpendicular to the axons (for a single coherent fiber bundle), respectively; $D_{||}$ and D_{\perp} are the parallel and perpendicular diffusion coefficients within the cylinder; R is the cylinder radius; and τ is half of the echo time. The noise floor is also estimated in the fitting procedure.

$$E(\mathbf{q}, \Delta) = f_h \cdot E_h(q, \Delta) + f_r \cdot E_r(q, \Delta) \quad (1)$$

where $E(\mathbf{q}, \Delta)$ is the measured signal decay; f_h and $E_h(q, \Delta)$ are the relaxation-weighted volume fraction and signal decay of the hindered part, respectively, whereas f_r and $E_r(q, \Delta)$ are the relaxation-weighted volume fraction and signal decay of the restricted part, respectively.

The CHARMED framework can be expanded to include additional hindered and restricted compartments, for example, allowing for N distinct fiber populations, we use:

$$E(\mathbf{q}, \Delta) = f_h \cdot E_h(q, \Delta) + \sum_{j=1}^N f_r^j \cdot E_r^j(q, \Delta) \quad (2)$$

where f_r^j and $E_r^j(q, \Delta)$ are the relaxation-weighted volume fraction and signal decay of the j th restricted compartment, respectively (Assaf et al., 2004).

The experimental data were fit to the model using code written in Matlab© (The Mathworks), which employs a non-linear least-square estimation procedure (utilizing Levenberg–Marquardt minimization). We used 3 configurations of CHARMED given in Eq. (2) to describe the measured data:

1. One hindered compartment and no restricted compartments ($N = 0$). This is identical to DTI analysis.
2. One hindered compartment and one restricted compartment ($N = 1$). This was used in areas of homogeneous white matter (e.g., corpus callosum).
3. One hindered compartment and two restricted compartments ($N = 2$). This was used in areas of crossing white matter fascicles.

Those 3 configurations were chosen first to compare DTI results and CHARMED results in areas of homogenous white matter (configuration 1 vs. 2). Second, in order to show the utility of CHARMED in areas of crossing white matter, we have used configuration no. 3 which includes restricted diffusion components. Using the parameters estimated from the fitting procedure, we then resampled $E(\mathbf{q})$ on a uniform grid in 3-D q space. A 3-D Fast Fourier Transformation (FFT) was applied to this data in order to obtain the average propagator, $\bar{P}_s(\mathbf{R}, \Delta)$ (Callaghan, 1991; Cory and Garraway,

1990) (i.e., the 3-D displacement probability function), which we used to produce 3-D iso-probability surfaces or 3-D contours in Matlab. Fitting was done on a pixel-by-pixel basis ranging from 2–5 min per pixel. For a slice of 64×64 pixels with approximately 2500 brain pixels, total computation time was about 2 h.

Cone of uncertainty simulations

To assess the variability of the computed fiber tract orientation, we performed simulations to measure the cone of uncertainty according to Jones et al. (Jones, 2003). Simulated DW data were produced for a one-fiber system lying on the z axis and for two-fiber bundles crossing orthogonal to each other along the xz and $-xz$ directions. For each fiber alignment configuration, DW data were simulated 500 times, once using high b value parameters and once with low b value parameters. For both high and low b value data sets, the following parameters were used: 31 gradient sampling directions, 16 b value increments for each direction with diffusion time of 50 ms and gradient duration of 45 ms. The signal-to-noise ratio was also varied in the simulation from infinity to 1. The maximal gradient amplitude for the high b value data set was 5 G/cm, and for the low b value data set, it was 1.25 G/cm, which results in b values of 12,681 s/mm² and 793 s/mm², respectively.

The CHARMED framework was used to fit the simulated signal decays. For the low b value data sets, we used CHARMED with only 1 hindered compartment (DTI) for the single-fiber data and 2 hindered compartments (dual-tensor) for the two-fiber data. For the high b value data sets, we used CHARMED with 1 hindered and 1 restricted compartment for the single-fiber data and 1 hindered and 2 restricted compartments for the two-fiber data. The 500 fits were used to calculate the 95% confidence level of the fiber orientation angle (Jones, 2003).

Results

Typical DWI data for one slice with different gradient directions and b values are shown in Fig. 1. For the $b = 1000$ and 500 s/mm² images, a b value range typically used for DTI, the changes in contrast with gradient orientation are already apparent; high signal intensity is seen where the diffusion gradients are applied perpendicular to the fiber direction while low signal intensity is observed elsewhere. This contrast increases greatly as the b value increases. At the highest b values, the only detectable signal in the DWI is in regions where the diffusion gradients are applied perpendicular to the fibers.

First, we compared conventional DTI analysis with CHARMED in regions having homogeneously oriented fiber bundles. We chose a small area at the level of the genu of the corpus callosum whose fibers connect the left to the right hemispheres. Fig. 2 shows an iso-probability surface plot of a DTI “diffusion ellipsoid” juxtaposed with a CHARMED “toothpick” for a region of interest (ROI) in the genu of the corpus callosum. The latter represents the iso-probability distribution from the restricted compartment obtained from CHARMED. The CHARMED “toothpick” is clearly more peaked than the diffusion ellipsoid. This means that for the same level of probability, water in the restricted pool diffuses a much smaller distance perpendicular to the fibers than in the hindered pool. By contrast, both pools diffuse similar distances parallel to the fibers. The CHARMED toothpick representation also provides

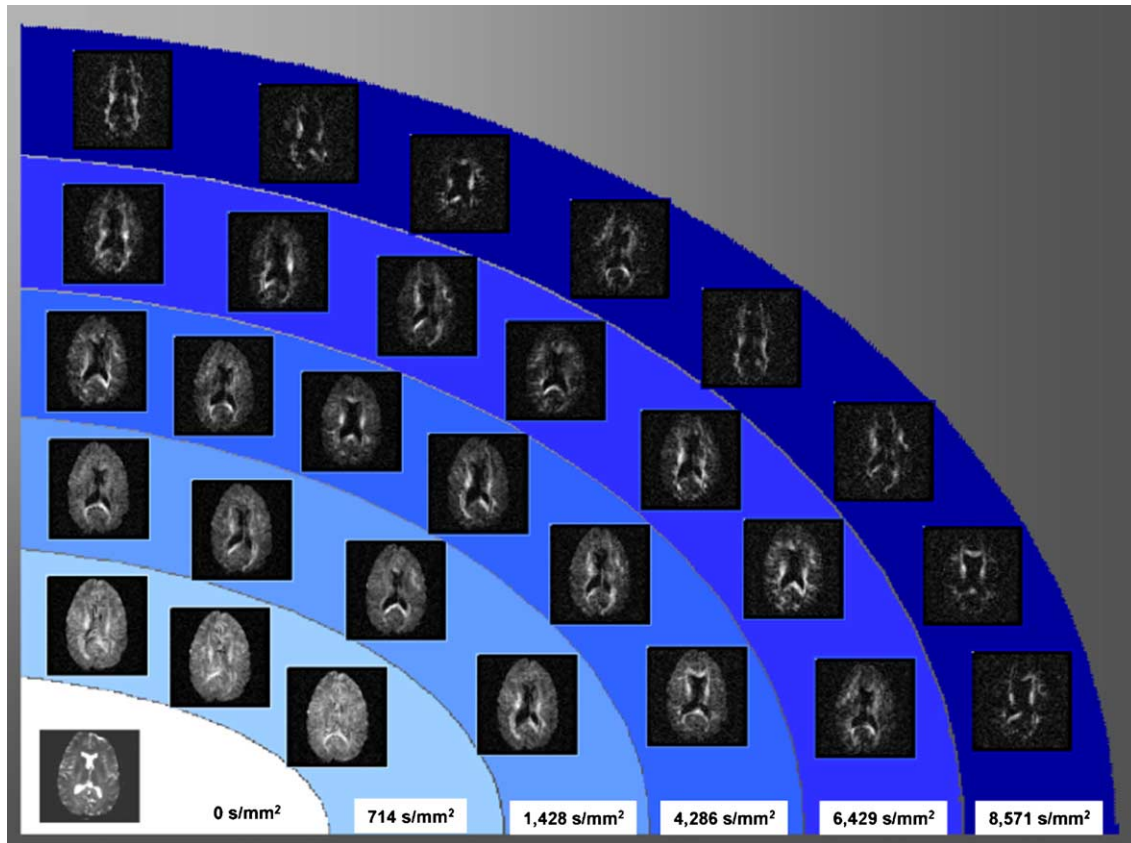


Fig. 1. Samples of the raw-data images. Data were collected at 10 shells of b value (only 6 are shown, more information given on Table 1) starting from 0 to 10,000 s/mm^2 . The angular resolution of gradient directions increased with the b value starting from 6 at the lowest (714 s/mm^2) up to 30 at the highest ($10,000 \text{ s/mm}^2$). Image quality was reasonable even at the highest b value shells (see darkest blue ring, $b = 8571 \text{ s/mm}^2$, $\text{SNR} > 5$) where signal originates only from white matter fibers placed perpendicular to the gradient direction.

greater dynamic range than the DTI ellipsoid in distinguishing among white matter, gray matter, and cerebrospinal fluid (CSF). Where in DTI the ellipsoid becomes spherical in gray matter and white matter, the CHARMED toothpick becomes very small when no restricted compartment is identified.

In a previous *in vitro* study, CHARMED revealed multiple white matter fiber orientations in pixels (Assaf et al., 2004). In order to estimate the ability of CHARMED to discriminate between more than one fiber bundle *in vivo*, we considered an ROI in human brain with a well-characterized fiber geometry and having known relative orientations. The corpus callosum and cingulum bundle are white matter fiber pathways oriented at 90° with respect to each other (Fig. 3). The fibers of the corpus callosum cross the brain from left to right whereas the cingulum bundle arches over the corpus callosum with its fibers crossing the brain from anterior to posterior (Figs. 3 and 4). Usually with high-resolution DTI, these two pathways can easily be separated (Fig. 4), particularly when using direction-encoded color mapping (Pajevic and Pierpaoli, 2000). However, here, we purposely combined these pathways into a single slice to see if CHARMED could separate them correctly. We combined raw data from two axial slices—one that contains the top edge of the corpus callosum and one above it that contains the cingulum bundle. In this way, we could analyze each fiber system separately as well as test the ability of CHARMED to resolve the individual pathways in the combined DWI data set. Fig. 5 shows DTI Direction-Encoded Color maps of the three data sets (i.e., the

corpus callosum, cingulum, and combined). Fig. 5A (enlarged at Fig. 5D) depicts the slice at the level of the corpus callosum, indicated in red (representing fibers crossing left and right), whereas the cingulum bundle at Fig. 5B (enlarged at Fig. 5E) is identified in green (representing fibers crossing up and down). In the combined data set (Fig. 5C, enlarged at Fig. 5F) the color in the area of the corpus callosum and cingulum appears orange, consistent with it being a weighted average of Figs. 5A and B. This can be seen also in the DTI iso-probability ellipsoids given in Figs. 6A, B, and C for the corpus callosum, cingulum, and combined data set. As with DTI, CHARMED was able to compute the fiber directions in the data sets for the corpus callosum alone and cingulum alone (see Figs. 6D and E) using one hindered and one restricted compartment. Using a single hindered and two restricted compartments, CHARMED was able to distinguish between the two-fiber populations for the combined data set, and provide the correct orientation of the two crossing fibers (Fig. 6F).

CHARMED provides estimates not only of the orientations of one or more fiber populations, but also microstructural parameters and compartmental diffusion coefficients. Fig. 7 shows CHARMED analysis on an entire slice depicting images of the relaxation-weighted volume fractions of the restricted pool and hindered pools, respectively, the fractional anisotropy and mean ADC of the hindered pool. The diffusivity perpendicular to the fibers in the restricted pool is not observable in this experiment, and was fixed in our simulation.

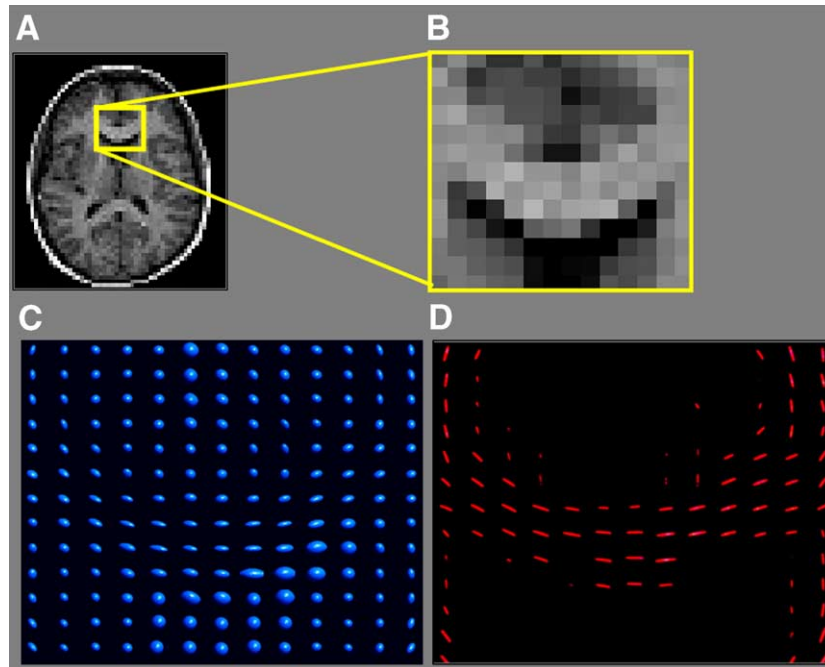


Fig. 2. (A) Low-resolution T_1 -weighted image of slice taken at the level of the lateral ventricles. (B) Enlargement of a region of interest surrounding the genu of the corpus callosum upon which CHARMED analysis was performed. (C) Iso-probability plots of the hindered component of CHARMED analysis (equal to DTI analysis). In areas of CSF and gray matter, the large spherical structures represent the isotropic diffusion, whereas in areas of white matter, the ellipsoids represent the orientation of the fibers. (D) Iso-probability surface plots of the restricted component of CHARMED. In areas of white matter, these plots look like 'toothpicks' aligned parallel to the fibers. The angular uncertainty in fiber orientation appears smaller in the restricted component plots than in the hindered component plots. In areas of CSF and gray matter, only a negligible fraction of restricted diffusion is found and when scaled to the fraction in gray matter, it is not observable in the iso-probability surface plots.

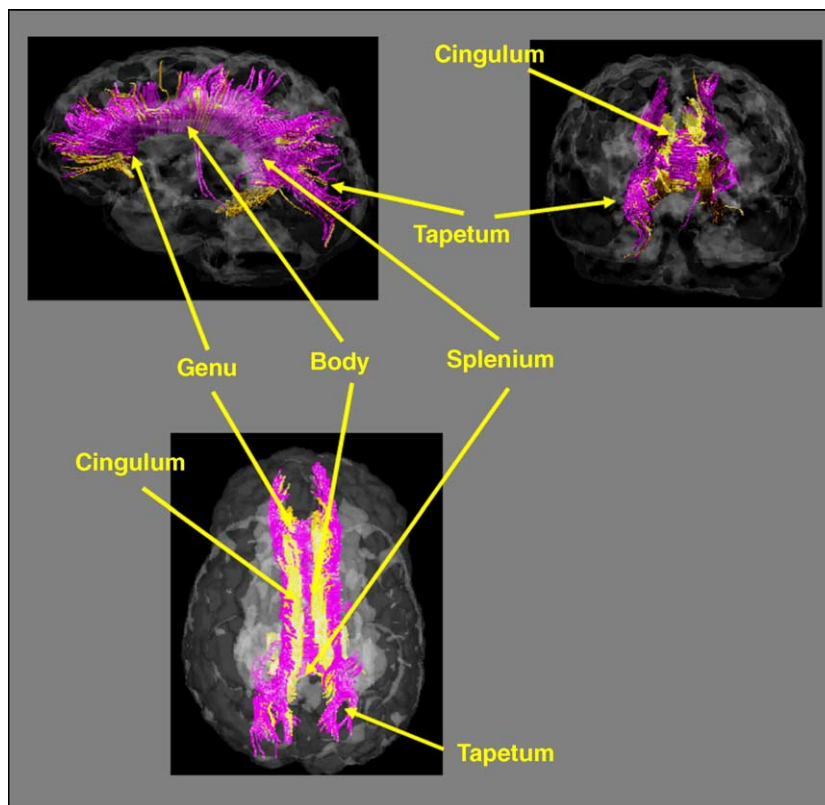


Fig. 3. Diffusion-tensor-based fiber tract images of the corpus callosum and cingulum fiber bundles. These two-fiber systems are orthogonal to each other where the cingulum lies on top of the corpus callosum. The fiber tract images were constructed from a whole brain diffusion tensor imaging data set. Seed regions of interest for fiber tracts were placed on mid-sagittal views for the corpus callosum and axial views above the corpus callosum for the cingulum.

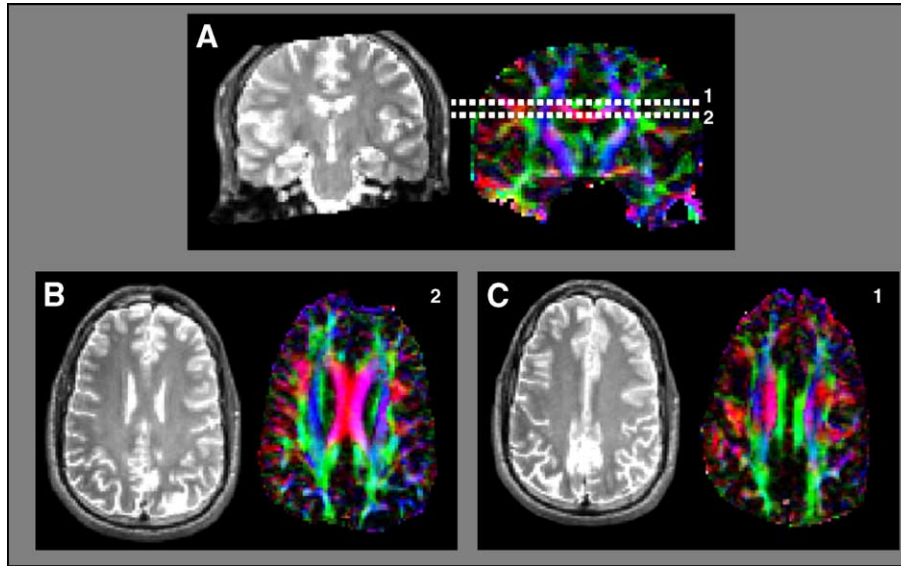


Fig. 4. T₂ and direction-encoded color maps of a healthy volunteer. (A) A coronal view showing the corpus callosum and cingulum. Lines represent axial slice locations given in panels B and C. (B) Axial T₂ and DEC images at the level of the corpus callosum. (C) Axial T₂ and DEC images at the level of the cingulum.

We also determined the relationship between DTI and CHARMED using simulations of the cone of uncertainty (see Methods). Fig. 8 shows simulations of the cone of uncertainty as a function of the SNR for a single fiber for DTI and CHARMED. Fig. 9 shows the same but for the two-fiber data modeled by a dual tensor (Inglis et al., 2001; Tuch et al., 2002) and CHARMED framework with one hindered and two restricted compartments. The cone of uncertainty is always smaller for CHARMED for any measured SNR. This effect is more significant when two distinct fiber populations are used. Then, the dual tensor model fails even at reasonable SNR (in the range of 10–20 typical of clinical

experiments). At low SNR (<5), both methods fail to provide accurate results of the fiber orientations.

Discussion

High *b* value diffusion imaging is increasingly used for delineating white matter structures in development and degeneration (Assaf et al., 2002a,b,c; Clark and Le Bihan, 2000; DeLano and Cao, 2002; Mulkern et al., 2001). In recent years, effort has been invested in developing analysis tools for such data (Alexander

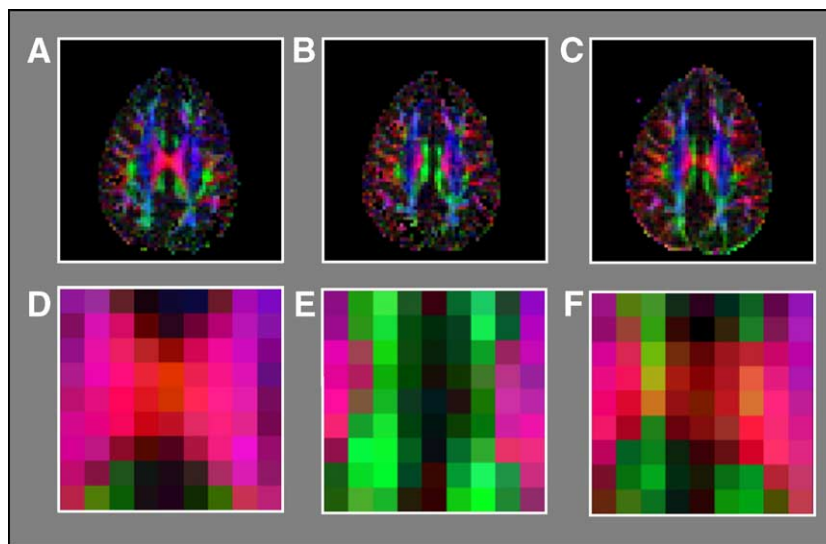


Fig. 5. Direction-encoded color maps of (A) an axial slice at the level of the corpus callosum, (B) an axial slice at the level of the cingulum (ci), and (C) an axial slice generated by combining data from slices (A) and (B). Enlargement of a region of interest showing mainly the corpus callosum and cingulum fibers for panels A, B, and C given in panels D, E, and F, respectively. In the combined images (C and F), the directionality calculated in the area of the corpus callosum and cingulum seems to be the weighted average of the two and does not represent the direction of either of the fibers (see orange–yellow areas in panel F).

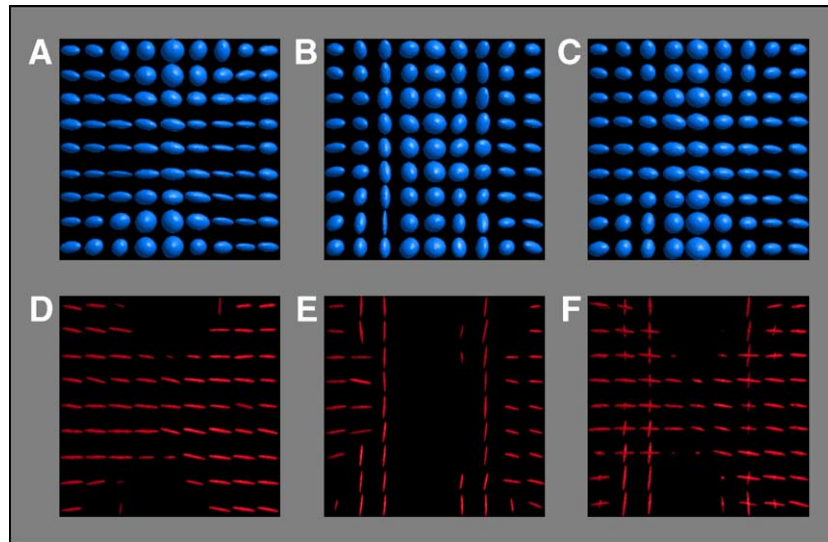


Fig. 6. Iso-probability surface plots of the slices given in Figs. 5D, E and F. (A–C) Iso-probability surface plots of the hindered part of CHARMED analysis. In the high-resolution slices (Figs. 5D and E) the orientation of the two-fiber system is well defined (see panels A and B). In the combined slice (Fig. 5F), the surface plots provide the weighted average of the fibers, making the diffusion ellipsoid more spherical in those regions. (D–F) Iso-probability surface plots of the restricted part of CHARMED analysis. In the high-resolution slices (comparable to Figs. 5D and E) the ‘toothpick’ shapes depict the two-fiber system. In the combined slice (comparable to Fig. 5F) in areas where the two systems cross, CHARMED was able to reconstruct the two systems with high accuracy.

et al., 2002; Assaf et al., 2000; Frank, 2002; Tuch et al., 2003; Wedeen et al., 2000). In this work, we demonstrate that high b value DWI data of human brain white matter in vivo can be characterized with CHARMED. The model assumes that, at high b values, the physical process that dominates the signal decay is restricted diffusion, while at low b values, hindered (Gaussian)

diffusion is more significant. When CHARMED was tested on phantom and excised spinal cord, it provided a clean separation between restricted and hindered processes (Assaf et al., 2004). This result validated the main assumption of the model that the major restricted compartment in white matter comes from intra-axonal water. To that end, the axonal inner membrane serves as a reflecting boundary for water molecules. In this case, under the long-time limit (i.e., mean free path in water is greater than the axonal radius), water diffusion perpendicular to the axon’s main axis will appear restricted.

CHARMED and human data

The simplest form of CHARMED, describing homogeneous white matter (i.e., a single bundle of fibers lying within a pixel), has 12 free parameters. In pixels containing heterogeneous white matter having two (or more) crossing fiber bundles, the number of free parameters increases to 15 and above. Estimating these parameters for an excised tissue sample requires acquisition of diffusion-weighted MR data having many different b values and gradient directions. Applying this model to the human brain in vivo is more challenging, not only because of the need to minimize the number of diffusion-weighted images acquired, but also for the following reasons: (A) We showed that, for crossing fibers, more than 20 directions are needed to distinguish fiber pathways accurately. (B) The higher sampled b values, the better estimate of the restricted compartment parameters. (C) At high b values, the signal to noise (SNR) decreases so more samples are required to maintain the data quality. Low-resolution sampling of q space in terms of gradient directions, b values, or poor SNR will degrade model parameter estimates (Assaf et al., 2004). By contrast, high-resolution sampling of q space causes extremely long acquisition times that will not satisfy clinical scanning requirements.

Here, we propose a pragmatic experimental protocol for CHARMED, which balances the various needs and requirements

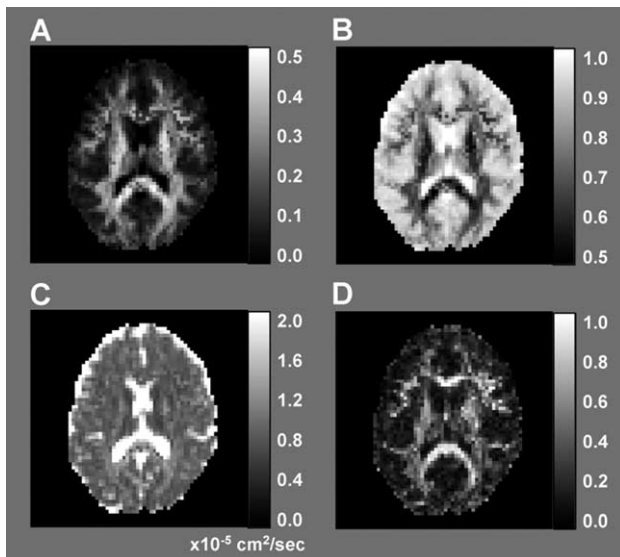


Fig. 7. CHARMED analysis on an entire slice. (A) Population fraction of the restricted components. High intensity is seen in areas of white matter, lower in gray matter, and none in CSF. (B) Population fraction maps of the hindered component. The image is a mirror image of panel A as all components are summed to 1; hence, white matter seems to have lower intensity than gray matter and CSF. (C) Mean diffusivity map calculated from the diffusion tensor eigenvalues of the hindered part of CHARMED. (D) Fractional anisotropy map calculated for the diffusion tensor eigenvalues of the hindered part of CHARMED.

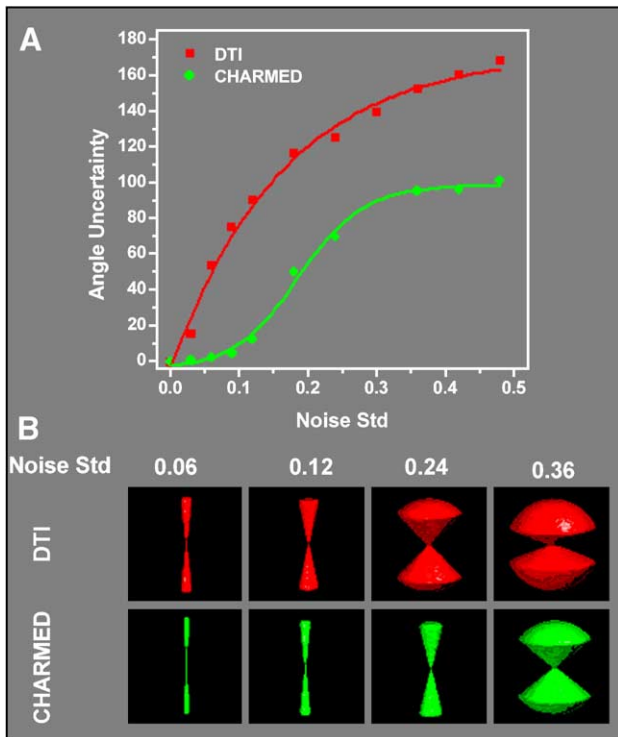


Fig. 8. (A) Angular uncertainty as a function of the noise standard deviation (Noise Std— σ_{std}) for simulated single-fiber data, calculated according to Jones (2003). Red dots represent angle uncertainty values calculated using DTI analysis of low b value data set and green dots represent the same but for CHARMED analysis of high b value data set. Red and green lines and the sigmoidal curve fit are given to guide the reader and emphasize the differences between the two analysis methods. (B) Cone of uncertainty surface plots given at 4 levels of noise standard deviation (0.06, 0.12, 0.24, and 0.36) for a simulated single-fiber data analyzed using DTI (red) and CHARMED (green). As signal was normalized to 1 in the simulation, the signal-to-noise ratio (SNR) is simple $1/\sigma_{\text{std}}$. For the cone of uncertainty surface plots, the SNR was 16.7, 8.3, 4.2, and 2.8 for $1/\sigma_{\text{std}}$ of 0.06, 0.12, 0.24, and 0.36, respectively.

described above. On one hand, the experimental design entails high angular resolution diffusion gradient sampling at high b values (30 directions), but on the other hand, low angular resolution (6 directions) at low b values. Low b value data is used primarily to fit a single diffusion tensor for which 6 directions are sufficient (Basser and Pierpaoli, 1998). To increase the angular resolution, we used 10 shells of b values in the range of 0–10,000 s/mm^2 , each of these shells was acquired using a different isotropic directional scheme. It is important to note that we are not using a conventional high angular resolution diffusion imaging (HARDI) scheme that entails sampling only a single shell in q or b space (Tuch, 2004; Frank, 2001). In addition, we used a 3-T scanner that provides high-quality diffusion-weighted image data even at high b values (>5000 s/mm^2). The clinical CHARMED acquisition framework thus provides high angular resolution only where it is needed, using a moderate number of diffusion-weighted acquisitions (192) with a reasonable SNR (even at highest b value, see Fig. 1).

CHARMED model parameters

The CHARMED model yields estimates of microstructural and physical parameters for the restricted and hindered compartments.

The hindered component provides diffusivities that resemble DTI analysis at low b value mainly since this component is modeled by a diffusion tensor. The restricted component provided high discrimination between gray matter, white matter, and CSF. The CSF, which has high diffusivity, appears dominant at the hindered (DTI) iso-probability plots (see Fig. 2). By contrast, CSF does not appear at the iso-probability plots of the restricted part as no restricted diffusion is measurable there (see Figs. 2 and 7). Moreover, in gray matter, the population fraction of the restricted component is much lower than in white matter (see population fraction maps, Fig. 7), suggesting that restricted diffusion is more apparent in white matter.

One of the advantages of CHARMED is that it can provide information about multiple fiber orientations within the same pixel (Assaf et al., 2004). We tested this using a thick slice containing fibers from both the corpus callosum and cingulum bundle and also on higher-resolution data with slices containing only the cingulum bundle or the corpus callosum. These two fibrous structures lie orthogonal to each other, and if sampled at low-enough resolution, can provide a model of orthogonal crossing fibers within the same pixel (see Figs. 3 and 4). In this case, conventional DTI provides a

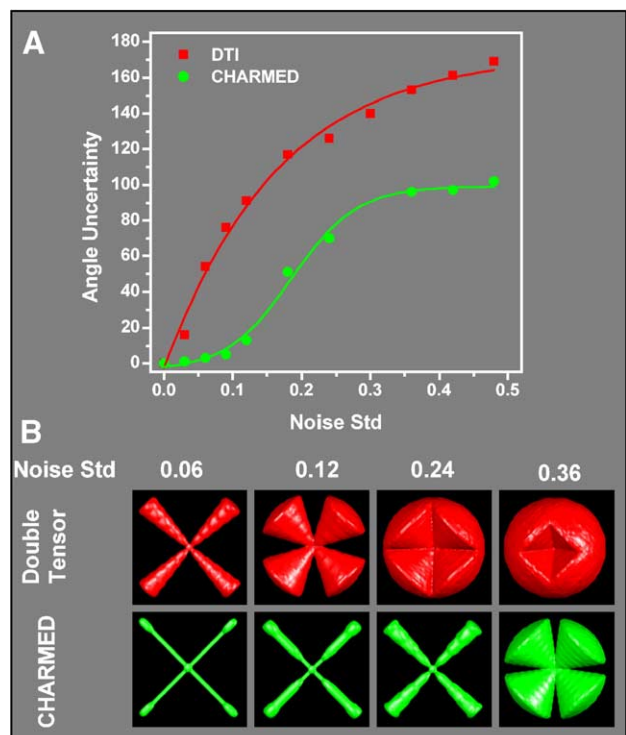


Fig. 9. (A) Angular uncertainty as a function of the noise standard deviation (Noise Std— σ_{std}) for simulated MR data for two crossing fibers. The angular uncertainty was calculated according to Jones (2003). Red dots represent angle uncertainty values calculated using dual tensor analysis of low b value data set and green dots represent the same but for a 2-restricted compartment CHARMED analysis of high b value data set. Red and green lines and the sigmoidal curve fit are given to guide the reader and emphasize the differences between the two analysis methods. (B) Cone of uncertainty surface plots given at 4 levels of noise standard deviation (0.06, 0.12, 0.24 and 0.36) for simulated two-crossing-fiber data analyzed using dual tensor (red) and CHARMED (green). As the signal was normalized to 1 in the simulation, the signal-to-noise ratio (SNR) is simply $1/\sigma_{\text{std}}$. For the cone of uncertainty surface plots, the SNR was 16.7, 8.3, 4.2, and 2.8 for $1/\sigma_{\text{std}}$ of 0.06, 0.12, 0.24, and 0.36, respectively.

powder average of the two fiber populations, producing an estimate of the fiber direction lying between the two direction vectors of the individual tracts (see Fig. 5). Using CHARMED with two restricted components, it was possible to extract the directions of the two fiber populations (see Fig. 6) with high accuracy. This is encouraging, since DTI tractography methods often fail to trace fiber tracts in regions where tracts cross.

To estimate the ability of CHARMED to separate crossing fibers and more generally to compare its angular resolution to DTI, we conducted a series of simulations at different SNRs and computed the cone of uncertainty. Surprisingly, at any given SNR, the cone of uncertainty was smaller for CHARMED than for DTI, implying that CHARMED provides higher angular definition (see Figs. 8 and 9). This is even more impressive since CHARMED uses high b value images in which SNR is extremely poor. Based on these simulations, it is not surprising that the CHARMED model was able to separate crossing fibers in the human brain. Moreover, even on the level of a single-fiber bundle, high b value CHARMED MRI provides better angular resolution for fiber tracking than DTI. This result supports our main assumption that restricted diffusion of intra-axonal water dominates the signal at high b value. As these water molecules are trapped within the axon, this displacement profile which is strongly biased perpendicular and parallel to the axon direction, will improve our estimate of local fiber orientation.

Analysis approaches to high b value data

Several approaches have been suggested to analyze high b value data, which can be divided into those that fit the data to a particular model and those that are “model free”. Among the “model-free” approaches, there is q space imaging (QSI) (Assaf et al., 2000; King et al., 1997), diffusion spectrum imaging (DSI) (Wedeen et al., 2000), high angular resolution diffusion imaging (HARDI) (Tuch, 2004; Frank, 2001), Q-ball imaging (QBI) (Tuch et al., 2003), and persistent angular structure MRI (PASMRI) (Alexander, 2004). QSI uses a 1-D Fourier transformation of the signal attenuation data acquired along several directions to obtain an estimate of width of the 1-D displacement distribution perpendicular to the fibers (Assaf et al., 2002a). Although this methodology is relatively fast in terms of acquisition times (~ 15 min for 10 slices at 3 T), it does not provide full characterization of the displacement profile in 3-D and hence may not be useful for fiber tracking and other applications. Nevertheless, QSI was shown to be extremely useful for following fine white matter degeneration in multiple sclerosis and dementia (Assaf et al., 2002a,b). By contrast to QSI, DSI (based on q space MRI method proposed by Callaghan, 1991) provides a 3-D characterization of the average propagator but requires sampling the \mathbf{q} vector in a regular grid over all of q space (Tuch et al., 2003; Wedeen et al., 2000). This approach is costly in terms of acquisition time. HARDI, Q-ball imaging, and PAS-MRI provide an orientational distribution function (ODF) for a DWI data set sampled at one particular high b value (typically 5000 s/mm²) sampled along many diffusion gradient directions. HARDI, Q-ball imaging, and PAS-MRI all provide an indication of white matter structure in areas where the fiber architecture is complex (e.g., crossing fibers), but with significantly shorter acquisitions times than required by DSI. None of these methods account for the effect of the “fat” or long-duration gradient pulse, which can distort features of the measured displacement distribution (Mitra and Halperin, 1995).

The most basic (and popular) model used to analyze the apparent bi-exponential decay observed at high b values is the dual tensor model (Assaf and Cohen, 1998; Clark and Le Bihan, 2000; Maier et al., 2001; Niendorf et al., 1996; Ronen et al., 2003). Here, two tensors are used to describe the signal decay. This model assumes two non-exchanging pools of water molecules: one exhibiting fast diffusion and the other exhibiting slow diffusion. This approach has produced results that are difficult to interpret physically, since it has repeatedly predicted that 20% of the water molecules in white matter exhibit extremely slow diffusion ($< 1 \times 10^{-7}$ cm²/s) and 80% of the water molecules exhibit fast diffusion (Niendorf et al., 1996). However, work by Nicholson and Sykova (1998) suggests that the ratio of extracellular to intracellular space is 20%/80%. The obvious conclusion is that extracellular diffusion is slow and intracellular diffusion is fast which is counterintuitive.

This conundrum is resolved if, however, restricted water diffusion within the axons is responsible for the slow component of the exponential decay (Assaf et al., 2002a). If this is the case, the Stejskal–Tanner or DTI model of diffusion is no longer valid since the assumed Gaussian displacement distribution does not hold. Moreover, above $b = 10,000$ s/mm², the decay becomes tri-exponential and eventually multi-exponential (Assaf and Cohen, 1998), supporting the conjecture that the origin of this signal is restricted diffusion. To that end, CHARMED assumes that the majority of the ‘slowly diffusing’ spins are undergoing restricted diffusion within the neuronal fibers. Although some restricted diffusion may also be apparent in the extra-axonal space, under normal physiological conditions, this appears negligible compared to that in the intra-axonal space. Support for this assertion comes from the population fraction maps (see Fig. 7) where the relative population fraction of the restricted component in gray matter (in which the fiber density is much smaller than white matter) is less than 10% of that in white matter.

Exchange and restricted diffusion

The present model assumes no exchange between hindered and restricted compartments. Exchange between different compartments has been studied with various models and methodologies and there is no agreement on the exchange rates of water molecules residing in the intracellular, intra-axonal, or extracellular compartments. While Pfeuffer et al. reported fast exchange in glial cells in early studies (Pfeuffer et al., 1998), more recently, much longer exchange times were reported (Meier et al., 2003; Sehy et al., 2002). This would suggest that water in glia might be restricted, rather than hindered (Lee and Springer, 2003). If water in the glia were restricted and contributed significantly to the total MR signal, we would expect to see a “slow” signal decay that would be independent of gradient direction, characteristic of restricted diffusion in porous media, such as in spherical pores (Hayden et al., 2004) or in spherical yeast cells (Cory and Garroway, 1990). However, experimentally, the decay in the signal attenuation does not support the existence of a significant isotropic restricted compartment. We do not see such signal decay in our data. Accordingly, we have chosen the simplest model with the fewest free parameters, which is nonetheless physically motivated to describe the signal decay we measure. Thus, our model currently does not include glia as a separate, restricted compartment, but rather lumps together water in glia and in the extracellular matrix. In our model, we assume that during a typical experimental diffusion time (on the order of 50–100 ms), water molecules

exchange freely between intra- and extracellular compartments through the semi-permeable cell membranes in glia at a rate of 25–50 ms. This exchange will cause both intracellular and extracellular compartments to appear as one compartment at long diffusion times. With respect to exchange between the intra-axonal space and the surrounding extracellular matrix and glia, it is reasonable to speculate that one myelin lamella will have a similar permeability to water molecules as a lipid membrane. However, when tightly packed and spirally arranged, the exchange between the intra-axonal and extra-axonal compartments should be extremely long. Studies show that this exchange rate may be as high as 700 ms, which under the typical experimental diffusion time (50–100 ms), will result in restricted diffusion of the intra-axonal compartment (Meier et al., 2003). This also implies that both components (hindered and restricted) are in the no-exchange limit, thus supporting our assumption about exchange between them.

The assumption of slow exchange between intra-axonal compartments has important implications for the formulation of CHARMED. As we assume that water diffusion in the intra-axonal compartment is restricted and its exchange is slow, exchange between different axons will also be slow if it occurs at all. This means that we can treat different fiber bundles as separate compartments. Using this assumption, we were able to use a multi-restricted model to fit pixels in which crossing fibers appear (see Fig. 6).

Finally, it is important to note that the hindered model describing water diffusion in the extra-axonal space is fairly insensitive to exchange. Whether there is fast exchange between different hindered compartments or no or slow exchange between them, the diffusion tensor model still can be applied (Basser, 2002) in the low-*b* or low-*q* regime.

Conclusions

The CHARMED MRI framework relates physiological and structural features to the MR signal decay in diffusion experiments measured over a large range of *b* values and diffusion gradient directions. CHARMED has two main assumptions: (A) Exchange between intra- and extra-axonal water pools is slow. (B) The majority of water exhibiting restricted diffusion in white matter originates from intra-axonal spaces. Using these assumptions, we are able to estimate various parameters from diffusion-weighted MR data, such as hindered compartment diffusivities and the population fraction of the restricted and hindered compartments. These parameters, especially the population fraction of the restricted component, might be very sensitive to various pathologies of white matter that involve myelin, the number of fibers, or intra-axonal composition. In the present examples, two fitting parameters were fixed in the model: the diffusivity of the restricted compartment perpendicular to the fibers and the axonal diameter distribution. Future work will aim at measuring these two quantities and exploring their use as possible image contrast mechanisms.

Acknowledgments

The authors thank the Adams Super Center for Brain Research of Tel Aviv University and the Ministry of Science and Technology of the State of Israel (The Eshkol program) for financial support (to Y.A.).

References

- Alexander, D., 2004. A comparison of q-ball and PASMRI on sparse diffusion MRI data. *Int. Proc. Soc. Magn. Reson. Med.* 13, 90.
- Alexander, D.C., Barker, G.J., Arridge, S.R., 2002. Detection and modeling of non-Gaussian apparent diffusion coefficient profiles in human brain data. *Magn. Reson. Med.* 48, 331–340.
- Assaf, Y., Cohen, Y., 1998. Non-mono-exponential attenuation of water and *N*-acetyl aspartate signals due to diffusion in brain tissue. *J. Magn. Reson.* 131, 69–85.
- Assaf, Y., Cohen, Y., 2000. Assignment of the water slow-diffusing component in the central nervous system using q space diffusion MRS: implications for fiber tract imaging. *Magn. Reson. Med.* 43, 191–199.
- Assaf, Y., Mayk, A., Cohen, Y., 2000. Displacement imaging of spinal cord using q space diffusion-weighted MRI. *Magn. Reson. Med.* 44, 713–722.
- Assaf, Y., Ben-Bashat, D., Chapman, J., Peled, S., Biton, I.E., Kafri, M., Segev, Y., Hendler, T., Korczyn, A.D., Graif, M., Cohen, Y., 2002a. High *b* value q space analyzed diffusion-weighted MRI: application to multiple sclerosis. *Magn. Reson. Med.* 47, 115–126.
- Assaf, Y., Kafri, M., Shinar, H., Chapman, J., Korczyn, A.D., Navon, G., Cohen, Y., 2002b. Changes in axonal morphology in experimental autoimmune neuritis as studied by high *b* value q space ¹H and ²H DQF diffusion magnetic resonance spectroscopy. *Magn. Reson. Med.* 48, 71–81.
- Assaf, Y., Mayzel-Oreg, O., Gigi, A., Ben-Bashat, D., Mordohovitch, M., Verchovsky, R., Reider Groswasser, I.I., Hendler, T., Graif, M., Cohen, Y., Korczyn, A.D., 2002c. High *b* value q space-analyzed diffusion MRI in vascular dementia: a preliminary study. *J. Neurol. Sci.* 203–204, 235–239.
- Assaf, Y., Freidlin, R.Z., Rohde, G.K., Basser, P.J., 2004. A new modeling and experimental framework to characterize hindered and restricted water diffusion in brain white matter. *Magn. Reson. Med.* 52, 965–978.
- Basser, P.J., 1995. Inferring microstructural features and the physiological state of tissues from diffusion-weighted images. *NMR Biomed.* 7–8, 333–344.
- Basser, P.J., 2002. Relationships between diffusion tensor and q space MRI. *Magn. Reson. Med.* 47, 392–397.
- Basser, P.J., Jones, D.K., 2002. Diffusion-tensor MRI: theory, experimental design and data analysis — A technical review. *NMR Biomed.* 456–467.
- Basser, P.J., Pierpaoli, C., 1996. Microstructural and physiological features of tissues elucidated by quantitative-diffusion-tensor MRI. *J. Magn. Reson.* B 111, 209–219.
- Basser, P.J., Pierpaoli, C., 1998. A simplified method to measure the diffusion tensor from seven MR images. *Magn. Reson. Med.* 39, 928–934.
- Basser, P.J., Mattiello, J., Le Bihan, D., 1994. MR diffusion tensor spectroscopy and imaging. *Biophys. J.* 66, 259–267.
- Callaghan, P.T. (Ed.), 1991. *Principles of Nuclear Magnetic Resonance Microscopy*. Oxford Univ. Press, Oxford.
- Clark, C.A., Le Bihan, D., 2000. Water diffusion compartmentation and anisotropy at high *b* values in the human brain. *Magn. Reson. Med.* 44, 852–859.
- Cory, D.G., Garroway, A.N., 1990. Measurement of translational displacement probabilities by NMR: an indicator of compartmentation. *Magn. Reson. Med.* 14, 435–444.
- DeLano, M.C., Cao, Y., 2002. High *b* value diffusion imaging. *Neuro-imaging Clin. N. Am.* 12, 21–34.
- Filley, C.M. (Ed.), 2002. *The Behavioral Neurology of White Matter*, 1st ed. Oxford Univ. Press, London.
- Frank, L.R., 2001. Anisotropy in high angular resolution diffusion-weighted MRI. *Magn. Reson. Med.* 45, 935–939.
- Frank, L.R., 2002. Characterization of anisotropy in high angular resolution diffusion-weighted MRI. *Magn. Reson. Med.* 47, 1083–1099.

- Hayden, M.E., Archibald, G., Gilbert, K.M., Lei, C., 2004. Restricted diffusion within a single pore. *J. Magn. Reson.* 169, 313–322.
- Inglis, B.A., Bossart, E.L., Buckley, D.L., Wirth III, E.D., Mareci, T.H., 2001. Visualization of neural tissue water compartments using biexponential diffusion tensor MRI. *Magn. Reson. Med.* 45, 580–587.
- Jones, D.K., 2003. Determining and visualizing uncertainty in estimates of fiber orientation from diffusion tensor MRI. *Magn. Reson. Med.* 49, 7–12.
- King, M.D., Houseman, J., Gadian, D.G., Connelly, A., 1997. Localized q space imaging of the mouse brain. *Magn. Reson. Med.* 38, 930–937.
- Lee, J.H., Springer Jr., C.S., 2003. Effects of equilibrium exchange on diffusion-weighted NMR signals: the diffusigraphic “shutter-speed”. *Magn. Reson. Med.* 49, 450–458.
- Maier, S.E., Bogner, P., Bajzik, G., Mamata, H., Mamata, Y., Repa, I., Jolesz, F.A., Mulkern, R.V., 2001. Normal brain and brain tumor: multicomponent apparent diffusion coefficient line scan imaging. *Radiology* 219, 842–849.
- Meier, C., Dreher, W., Leibfritz, D., 2003. Diffusion in compartmental systems: II. Diffusion-weighted measurements of rat brain tissue in vivo and postmortem at very large b values. *Magn. Reson. Med.* 50, 510–514.
- Mitra, P.P., Halperin, B.J., 1995. Effects of finite gradient-pulse widths in pulsed field-gradient diffusion measurements. *J. Magn. Reson.* 113, 94–101.
- Mulkern, R.V., Vajapeyam, S., Robertson, R.L., Caruso, P.A., Rivkin, M.J., Maier, S.E., 2001. Biexponential apparent diffusion coefficient parametrization in adult vs newborn brain. *Magn. Reson. Imaging* 19, 659–668.
- Neuman, C.H., 1974. Spin echo of spins diffusing in a bounded medium. *J. Chem. Phys.* 60, 4508–4511.
- Nicholson, C., Sykova, E., 1998. Extracellular space structure revealed by diffusion analysis. *Trends Neurosci.* 21, 207–215.
- Niendorf, T., Dijkhuizen, R.M., Norris, D.G., van Lookeren Campagne, M., Nicolay, K., 1996. Biexponential diffusion attenuation in various states of brain tissue: implications for diffusion-weighted imaging. *Magn. Reson. Med.* 36, 847–857.
- Pajevic, S., Pierpaoli, C., 2000. Color schemes to represent the orientation of anisotropic tissues from diffusion tensor data: application to white matter fiber tract mapping in the human brain. *Magn. Reson. Med.* 42, 526–540.
- Pfeuffer, J., Flogel, U., Dreher, W., Leibfritz, D., 1998. Restricted diffusion and exchange of intracellular water: theoretical modeling and diffusion time dependence of ¹H NMR measurements on perfused glial cells. *NMR Biomed.* 11, 19–31.
- Pierpaoli, C., Jezzard, P., Basser, P.J., Barnett, A., Di Chiro, G., 1996. Diffusion tensor MR imaging of the human brain. *Radiology* 201, 637–648.
- Ronen, I., Kim, K.H., Garwood, M., Ugurbil, K., Kim, D.S., 2003. Conventional DTI vs. slow and fast diffusion tensors in cat visual cortex. *Magn. Reson. Med.* 49, 785–790.
- Sehy, J.V., Banks, A.A., Ackerman, J.J., Neil, J.J., 2002. Importance of intracellular water apparent diffusion to the measurement of membrane permeability. *Biophys. J.* 83, 2856–2863.
- Stejskal, E.O., Tanner, J.E., 1965. Spin diffusion measurements: spin echoes in the presence of time-dependent field gradient. *J. Chem. Phys.* 42, 288–292.
- Tofts, P. (Ed.), 2003. *Quantitative MRI of the Brain: Measuring Changes Caused by Disease*, 1st ed. John Wiley and Sons.
- Tuch, D.S., 2004. Q-ball imaging. *Magn. Reson. Med.* 52, 1358–1372.
- Tuch, D.S., Reese, T.G., Wiegell, M.R., Makris, N., Belliveau, J.W., Wedeen, V.J., 2002. High angular resolution diffusion imaging reveals intravoxel white matter fiber heterogeneity. *Magn. Reson. Med.* 48, 577–582.
- Tuch, D.S., Reese, T.G., Wiegell, M.R., Wedeen, V.J., 2003. Diffusion MRI of complex neural architecture. *Neuron* 40, 885–895.
- Wedeen, V.J., Reese, T.G., Tuch, D.S., Wiegell, M.R., Dou, J.-G., Weiskoff, R.M., Chessler, D., 2000. Mapping fiber orientation spectra in cerebral white matter with Fourier transform diffusion MRI. *Proc. Intl. Soc. Magn. Reson. Med. ISMRM, California*, p. 82.